

Revealing the Mechanism Behind Sudden Capacity Loss in Lithium Metal Batteries

To cite this article: Meinan He *et al* 2023 *J. Electrochem. Soc.* **170** 100528

View the [article online](#) for updates and enhancements.

You may also like

- [Critical Current Density Measurements of Argyrodite \$\text{Li}_6\text{PS}_5\text{Cl}\$ Solid Electrolyte at Ambient Pressure](#)

Artur Tron, Ander Orue, Pedro López-Aranguren *et al.*

- [Ultrasound-Induced Impedance Reduction in Lithium Ion Batteries](#)

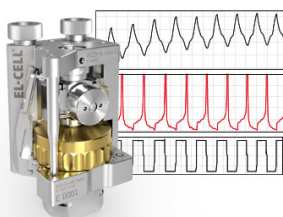
Ganghyeok Im, Derek Barnes, Wei Lu *et al.*

- [Review—Early Efforts to Develop Practical Rechargeable Lithium Batteries](#)

K. M. Abraham

Measure the Electrode Expansion in the Nanometer Range.
Discover the new ECD-4-nano!

EL-CELL[®]
electrochemical test equipment




- Battery Test Cell for Dilatometric Analysis (Expansion of Electrodes)
- Capacitive Displacement Sensor (Range 250 μm , Resolution ≤ 5 nm)
- Detect Thickness Changes of the Individual Electrode or the Full Cell.

www.el-cell.com +49 40 79012-734 sales@el-cell.com





Revealing the Mechanism Behind Sudden Capacity Loss in Lithium Metal Batteries

Meinan He,^{1,=} Charles Wampler,^{1,=} Louis G. Hector Jr.,¹ Michael Dato,²
Suryanarayana Kolluri,¹ Khalil Amine,² Chi-Cheung Su,^{2,z}  and Mei Cai^{1,z,*}

¹Battery Materials and Systems Research, General Motors Global Research and Development Center, Warren, Michigan 48090, United States of America

²Chemical Sciences and Engineering Division, Argonne National Laboratory, Lemont, Illinois 60439, United States of America

Rechargeable Li-metal batteries (LMBs) are attractive energy storage candidates for electric vehicles (EVs) because they offer higher energy density than batteries built with intercalation electrodes. However, one of the main barriers to the commercial deployment of LMBs has been their relatively short cycle life. Re-designing the electrolyte system shows promise in achieving acceptable cycle life, but even so, the resulting cells display a challenging end-of-life (EOL) behavior: a sudden capacity loss. Herein, we report a new method for analyzing voltage profiles during cycling to distinguish between the capacity loss originating from the loss of cathode capacity vs growth in cell resistance. This analysis reveals that sudden capacity loss was preceded by acceleration in the rate of growth of cell resistance, and cycling of multiple cells showed that this phenomenon is sensitive to the initial quantity of electrolyte in the cells. In contrast, the cathode capacity degraded at a constant rate independent of the electrolyte quantity. Combining this evidence with post-analysis of harvested electrolyte and electrodes, we conclude that neither the loss of active lithium nor the loss of active cathode material was the primary source of sudden capacity loss; instead, consumption and decomposition of electrolyte causes the drastic capacity loss at EOL.

© 2023 The Electrochemical Society ("ECS"). Published on behalf of ECS by IOP Publishing Limited. [DOI: [10.1149/1945-7111/ad01e7](https://doi.org/10.1149/1945-7111/ad01e7)]

Manuscript submitted July 17, 2023; revised manuscript received September 17, 2023. Published October 23, 2023.

Supplementary material for this article is available [online](#)

With increasing public concern about the environment, the development of the next generation energy storage technologies with high energy and low cost has become very urgent. Rechargeable Li-metal batteries (LMBs) have attracted considerable attention due to their greatly increased energy density,^{1–3} which can be as high as 500 Wh kg⁻¹, compared to only 250 Wh kg⁻¹ for Li-ion batteries built with graphite-based anodes.^{3–5} This advantage arises because an LMB charges by plating pure Li on the negative electrode instead of intercalating it into graphite. In fact, the theoretical capacity of lithium metal anodes is 3863 mAh g⁻¹, which is significantly higher than that of graphite (372 mAh g⁻¹).^{2,3,6–8} Moreover, the use of pure lithium not only eliminates the weight of the active graphite particles, but also eliminates the binders and other materials required to form a viable porous electrode.

While boasting high energy density, LMBs are prone to problematic dendritic growth of Li deposits during cycling, which can ultimately lead to device shorting and cell failure.^{8–11} To improve the performance of LMBs, a variety of strategies have been investigated, such as physically blocking the dendrite growth by using high-modulus solid electrolytes,^{12–14} adjusting the surface electric field to change the initial nucleation of Li deposition by using three-dimensional current collectors,^{15–17} and preventing the growth of Li dendrites via employing modified separators.^{9,10,18} Additionally, the development of an advanced non-aqueous electrolyte system to enhance the cycle life and cycling stability is also a cost-effective approach.^{19–23}

While the suppression of dendrites is a pre-requisite for acceptable cycling performance, shorting is not the only mode of failure. Most of the published LMB systems still exhibit sudden capacity decay at the end of their cycle lives, with capacity drops as high as 20% within 5 cycles being typical.^{9,24–26} The most probable causes of such failure are electrolyte dry-out, loss of active Li, and impedance build-up. There are many studies which document such phenomenon in myriad testing conditions.^{27–30} Especially for pouch cell configurations, there is interest in quantifying electrochemical

changes as predictors for EOL and associating them with either electrode. Namely, OCP cell resistance has been used to demonstrate continuous electrolyte decomposition on lithium metal.^{27,31} As there is little room for optimization of cell weight, investigating electrolyte-lean scenarios with electrolytes that have modified physical and chemical properties can be a way to simultaneously improve performance and safety for high voltage electrodes.

Sudden capacity failure imposes a challenge for the battery management system (BMS) in an EV, since it can cause an unexpected loss of range and might even leave a motorist stranded far from a charging station.^{32–34} If the phenomenon cannot be eliminated, it will be imperative that the BMS be able to predict it in advance so that the vehicle can be serviced proactively to avoid a walk-home situation. A deeper understanding of this sudden capacity failure may facilitate the development of reliable prognostic indicators.

In this work, the main cause of sudden capacity loss was determined to be consumption and decomposition of electrolyte for LMBs built with NMC cathodes and liquid fluorinated electrolyte. Three pouch-cell LMBs were cycled until failure, while each one began cycling with a different quantity of electrolyte. During cycling, the voltage and current data were collected for further analysis. After failure, the remaining electrolyte was quantified and the harvested, aged electrodes were evaluated. Each harvested electrode was coupled with a fresh opposing electrode and a fresh supply of electrolyte to test its true capacity loss. These procedures were complemented with our method for analyzing voltage profiles to distinguish between cathode capacity loss and the capacity loss that results from increased cell resistance. We show that the resistance estimated by this procedure is a promising indicator for the advance prediction of capacity failure. All of the post-mortem analysis results pointed to electrolyte dry-out as the main mode of failure. This finding together with our method for analyzing voltage profiles provide a critical tool for the accurate prediction of sudden capacity loss.

Experimental

Electrode fabrication.—The cathode slurry composition is 95% NCM811, 2.0 wt% Super P-Li, 0.2 wt% SWCNT, and 2.8 wt%

⁼Equal contribution.

*Electrochemical Society Member.

^zE-mail: csu@anl.gov; mei.cai@gm.com

Solvey 5130 polyvinylidene fluoride (PVDF) binder. The slurry was coated on a 12 μm aluminum current collector with 20 mg cm^{-2} single side solid or 40 mg cm^{-2} double side material loading. Furthermore, the as-fabricated electrode was pressed to a porosity of 25%, or 3.3 g cm^{-3} electrode density. The negative electrode was 20 μm Li metal foil on a Cu current collector purchased from Honjo Chemical Corporation.

Electrolyte preparation.—The electrolytes were prepared to follow the formulation disclosed in this report. Battery grade salt and solvents are purchased from Gotion and Soulbrain respectively. The moisture of the as-prepared solvent and electrolyte was below 20 ppm (determined by Karl Fischer titration). The electrolyte preparation was performed in an Ar-filled glovebox with controlled moisture content <2 ppm. The electrolyte formulated as 1.2 M LiPF_6 in 1:4 (v/v) fluoroethylene carbonate (FEC) and dimethyl carbonate (DMC).

Cell fabrication and testing.—A 2032 type coin cell was used for battery testing. LillNMC cells were assembled in the Ar-filled glovebox with Li metal foil on a Cu current collector as both the counter and reference electrodes. Entek Al_2O_3 filled microporous polyethylene (PE), was used as the separator. The effective diameters of cathode, anode, and separator were 14 mm, 15 mm, and 16 mm, respectively and the electrolyte injection amount is 30 μl .

Pouch Cells with a 5Ah capacity were fabricated with a $\text{LiNi}_0.8\text{Mn}_0.1\text{Co}_0.1\text{O}_2$ (NMC 811) cathode, a lithium anode with 20 μm of Li metal foil on an 8 μm Cu foil current collector. Entek Al_2O_3 filled microporous polyethylene (PE) was used as the separator. The liquid electrolyte was prepared in-house as described above. Pouch cells were constructed using a 6.0 cm by 5.0 cm punched cathode electrode and a 6.2 cm by 5.2 cm punched lithium anode, and a 6.5 cm wide separator. The anode was larger than the cathode to ensure full cathode coverage. Twenty-seven pieces of cathode and twenty-eight pieces of anode were stacked to assemble the pouch cell in a dry room (-40°C dew point). The testing pouch cells were filled with 2.2 g Ah^{-1} (cell 1), 2.0 g Ah^{-1} (cell 2) and 2.5 g Ah^{-1} (cell 3) of electrolyte respectively, and they were all rested for 24 h before testing.

Cycling protocol.—Electrochemical experiments were conducted on a Landt cycler (model# CT3001A) at 25°C . A relatively low stack pressure of 15 psi was applied uniformly on the cell during testing. Cells were first cycled at 500 mA (C/10) for both charge and discharge between 3.0–4.25 V for 2 formation cycles. After that, the cell was removed from the fixture for degassing and final sealing/trimming. The cell was then put back into the fixture with 15 psi pressure for cycling. The charge phase of each cycle was constant-current charge at 500 mA (C/10) to 4.25 V followed by a constant-voltage hold at 4.25 V, terminating at 100 mA (C/50). The discharge phase was a constant-current 2.5 A (C/2) to 3.0 V, with no voltage hold. After each charge and discharge cycle, the cell was rested at open circuit for 10 min before the next cycle. The voltage and current were sampled at a maximum time interval of 30 s or a voltage change of 1 mV, whichever came first.

Cell disassembly and scanning electron microscopy analysis.—The cycled cells were disassembled in an Ar-filled glovebox. The electrodes were thoroughly rinsed with anhydrous DMC and dried in a vacuum oven. The morphologies of the harvested electrodes were examined with scanning electron microscopy (SEM) using a Hitachi S-4800-II microscope.

NMR quantitative analysis.—To analyze the harvested electrolyte in a LillNMC cell by nuclear magnetic resonance (NMR) spectroscopy, acetonitrile- d_3 (3 mL) was used as the extracting solvent. The outer case of the cycled LillNMC cell was first washed with Dimethyl Carbonate (DMC) three times and vacuum dried

before being disassembled in a glove box. All parts of the dismantled cell were then transferred quickly into a vial of 3 mL acetonitrile- d_3 . The capped vial was then shaken vigorously for 1 minute to ensure the dissolution of the electrolyte. After that, the solution was partially transferred to an NMR tube for quantitative analysis. The amounts of FEC and DMC left in the cycled cells were quantified by comparing the integration of the proton peaks of FEC or DMC with the proton peak of acetonitrile. The NMR analyses were carried out on a 300-MHz NMR spectrometer. The spin lattice relaxation time (T_1) was measured by the inversion recovery method. The relaxation delay time (d1) of the acquisition was larger than the 5 T_1 time.

X-ray diffraction.—X-ray diffraction (XRD) on powder samples from pristine and aged cathodes was performed on a Hitachi diffractometer by using Cu ($K\alpha$) radiation. The 2 Theta range was selected from 10° to 90° and the scan rate was set to $2^\circ/\text{min}$.

Results and Discussion

Modeling and data analysis using voltage curves and constant-current capacity.—To predict the failure behavior, it is essential to create a reliable degradation model. We first attempted to establish such a degradation model using the voltage profiles and the cell capacities in different stages. The cyclers data consists of time-stamped current $I(t)$ and voltage $V(t)$, sampled every 30 s during constant-current (CC) operation and approximately every 10 s during rests and constant-voltage (CV) holds. Using amp-hour integration of the current signal, we obtain a discharge capacity for the i^{th} cycle of $q_i^D(t) = \int_{t_{0i}}^t I(\tau) d\tau$ with a final value of $Q_{CCi}^D = -q_i^D(t_{1i})$, where $t_{0i} \leq t \leq t_{1i}$ is the time span of the i^{th} discharge. Similarly, the charge phase of the i^{th} cycle, spanning $t_{1i} \leq t \leq t_{2i}$, gives $q_i^C(t)$, offset so that $q_i^C(t_{2i}) = 0$, whereupon $Q_{CCi}^C = -q_i^C(t_{1i})$. The signs on Q_{CCi}^D and Q_{CCi}^C make them positive, since we are using the convention that discharge current is negative.

Figures 1 and 2 show plots of voltage vs capacity for cells #1 & #2, respectively. Discharge curves are solid lines and charge curves are dashed. The vertical line segments show the recovery of voltage during the rest period at the end of each discharge. The 4.25 V constant-voltage segment at the top of charge is also clearly visible, growing in duration as the cell ages. The curves are plotted every 50th cycle until capacity failure starts, at which point we show each successive cycle. The curves are similarly shaped with the most notable differences occurring near the top of charge. Besides the trend of decreasing capacity, evident in where the curves hit the 3 V voltage floor, there is also a clear trend of increasing resistance. In fact, the spacing between discharge curves grows with age, as one may see for Cell #1, by comparing cycles 200, 250, and 300. In the last few cycles, the rate of capacity loss accelerated dramatically. For Cell #2, the same trend is obvious by comparing the gap between cycles 300 and 350, which is much bigger than the previous gap between cycles 250 and 300. This result indicates an acceleration of the decay rate.

Figure 3 shows the discharge and charge capacities, Q_{CCi}^D and Q_{CCi}^C , vs cycle number, i , for all three cells. For the first 300 cycles, they show a similar trend in capacity loss. The primary feature in this study is the sudden capacity failure, which begins at cycle 308 for Cell #1, cycle 390 for Cell #2, and cycle 377 for Cell #3. The extra electrolyte added to Cells #2 and #3 clearly extends their cycle life compared to the cycle life of Cell #1. Moreover, the charge capacity consistently exceeds the discharge capacity, although the Coulombic efficiencies of all three cells were at least 99.5% before failure.

Three factors can contribute to a decrease in constant-current capacity: a loss of active material (LAM) (a decrease in the cathode's intrinsic capacity), a loss of lithium inventory (LLI), and an increase in resistance. As illustrated in Fig. S1, in a plot of voltage vs capacity (V vs q), these factors would appear as follows.

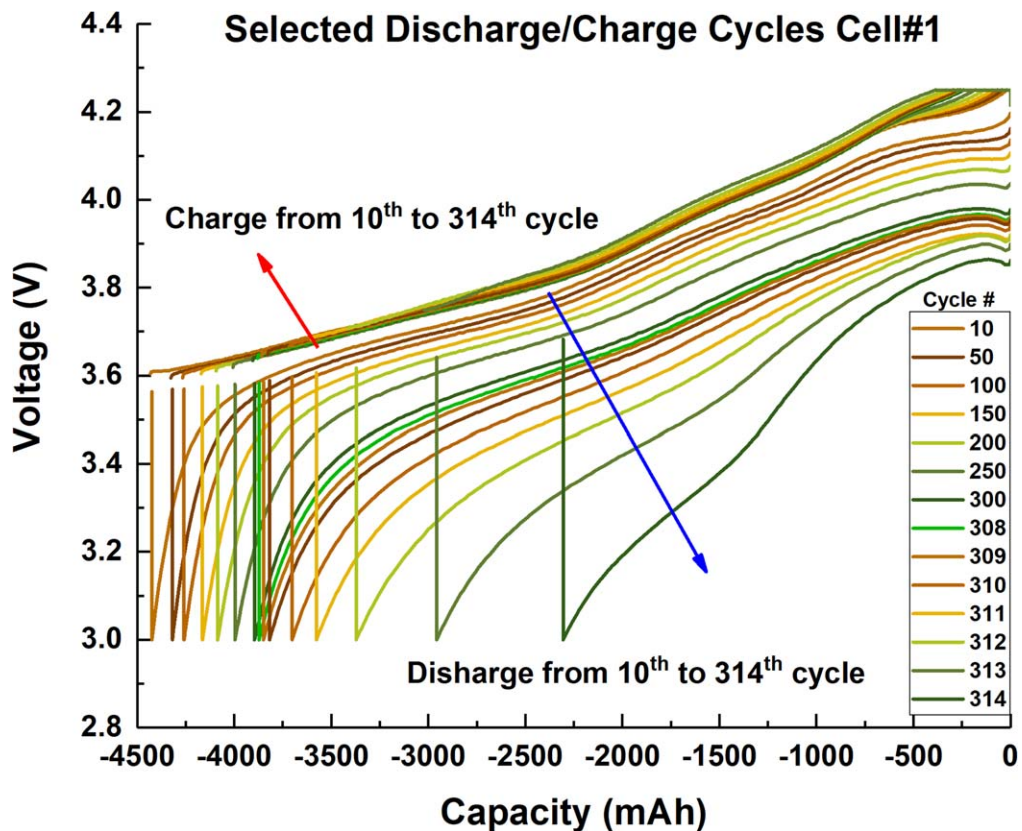


Figure 1. Selected cycles for Cell #1 (2.0 g Ah^{-1} electrolyte). The selected cycles advance by 50 until the onset of failure at cycle 308, after which every cycle is shown.

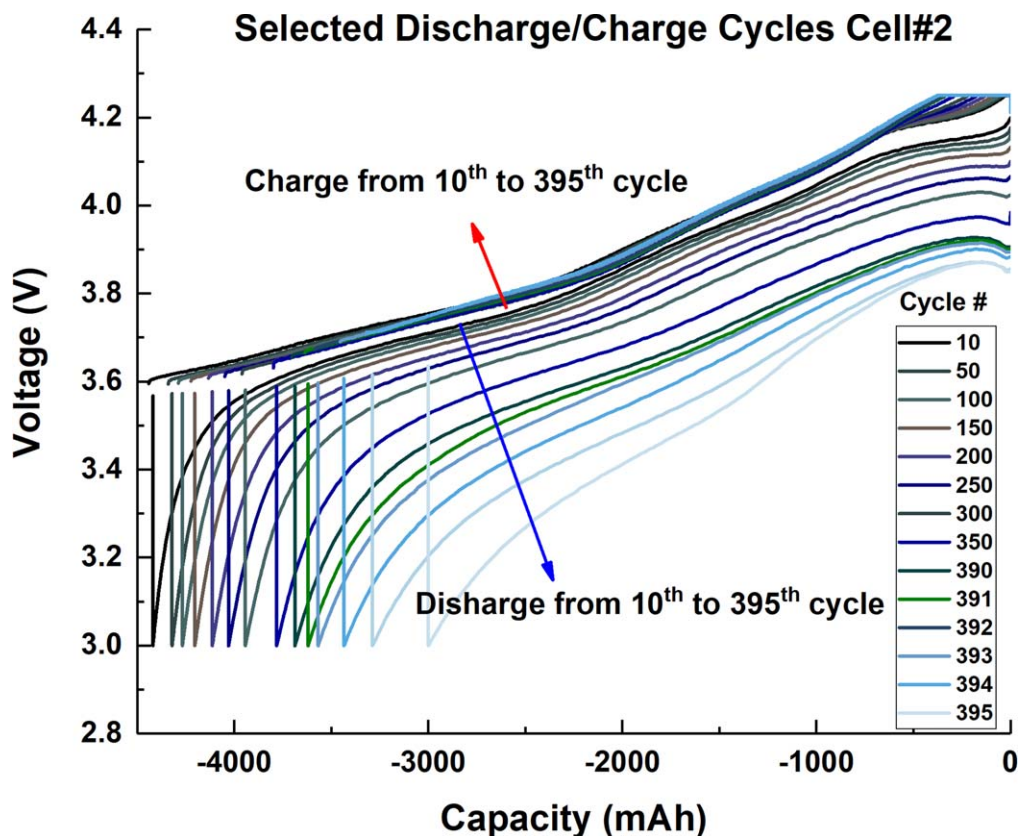


Figure 2. Selected cycles of Cell #2 (2.2 g Ah^{-1} electrolyte). The selected cycles advance by 50 until the onset of failure at cycle 390, after which every cycle is shown.

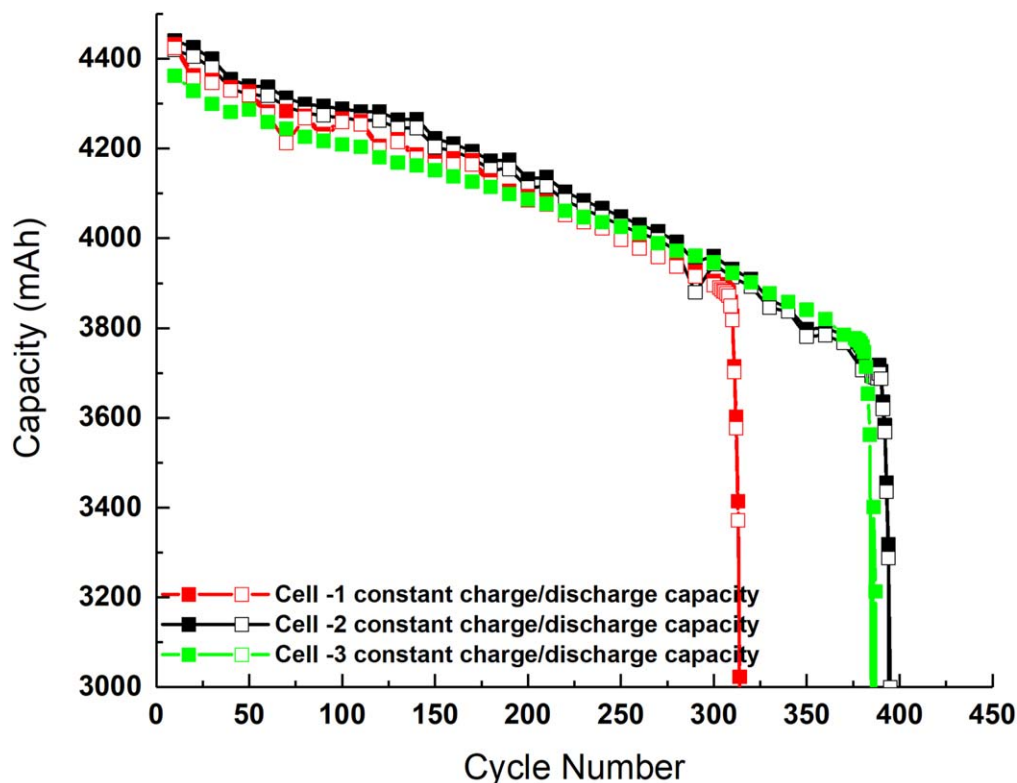


Figure 3. Constant-current capacities of discharge and charge for all three pouch cells. Our hypothesis is that the sudden drop-off at EOL is due to the electrolyte dry-out.

- LAM: A decrease in the cathode's capacity (red dot-dashed line) will appear as an increase in the slope, dV/dq .
- LLI: A loss of lithium inventory (yellow dot-dashed line) will have no effect until the initial excess lithium provided by the Li foil in the anode is used up. Once the cyclable lithium falls below the cathode capacity, the voltage curve will drop vertically at full discharge when the lithium anode hits empty.
- An increase in resistance (purple dash-dot line) will appear as a downward translation of the voltage curve.

One sees in Figs. 1 and 2 an obvious downward translation in the discharge curves as cycling proceeds. There is also evidence of an increase in slope in both charge and discharge curves. However, near the end of discharge, the voltage curve always smoothly transits over the "knee" of the curve, showing no evidence of a sudden drop. Consequently, we can eliminate LLI as a factor in our analysis: the sudden drop in capacity occurs before the lithium inventory ever falls below the cathode capacity.

To understand the situation more thoroughly, we would like to separate the influences of LAM and resistance growth. Our approach is summarized in Fig. 4.

Voltage model and open-circuit voltage estimate.—A basic model for cell voltage during constant-current operation consists of an open-circuit voltage curve (OCV) that describes near zero-rate operation plus resistive terms that depend on the C-rate. Lacking an independently measured OCV curve, we begin by estimating it from the voltage curve for an early cycle, assuming that the resistive component is linear in current. For the initial cycle in our model, we use the 10th experimental cycle to allow the initial material characteristics to settle. Let x be a state of charge coordinate defined as $x = 1$ when the cell is fully charged and $x = 0$ when the cell is at the lowest SOC attained in cycle 10. Finally, let Q_{tot} be the discharge capacity from $x = 1$ to $x = 0$, which represents a measure of the reversible thermodynamic capacity of the cell. In fact, Q_{tot} is always

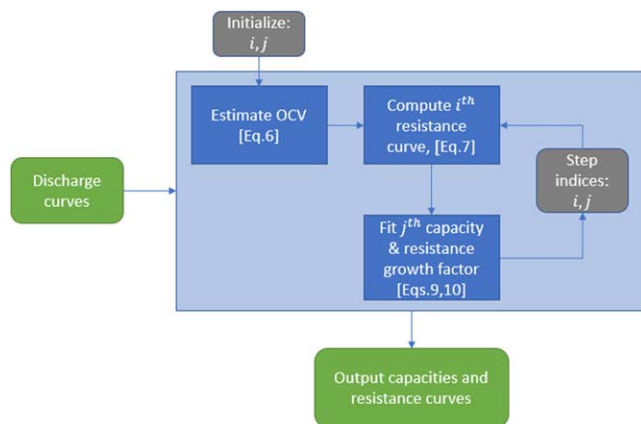


Figure 4. Flowchart of the analysis procedure.

greater than the constant-current capacity, which uses voltage as a cutoff condition and is therefore affected by the non-equilibrium voltage offset of irreversible resistance. Although Q_{tot} can be measured theoretically by using very low charging current ($C/100$) and including a long voltage hold at both limits, this measurement is highly impractical since it adds tremendous time to each cycle. Because we are using CC discharges and resistance increases with age, our experiments only reach $x = 0$ on the initial cycle. This means that while we observe the constant-current capacities Q_{CCi}^D for $i > 10$, we must infer the total capacities $Q_{toti} \geq Q_{CCi}^D$ from the measured discharge curves.

We expect Q_{tot} to decline monotonically with cycling. This means Q_{toti} can be used as a coordinate representing the aging of the cell. With current I in A and capacity Q_{tot} in Ah, we work with C-rate, $\hat{I} = I/Q_{tot}$, which has units $1/h$. For small current I , the

constant-current voltage response of the cell initiated from a fully rested state at 100% SOC can be modeled as a Taylor series in \hat{I} in Eq. 1:

$$V(x) \approx OCV(x) + \zeta(x)V_{gap}(x, Q_{tot}) + R_1(x, Q_{tot})\hat{I} + R_2(x, Q_{tot})\hat{I}^2 + \dots, \quad [1]$$

where x is SOC, OCV is the open-circuit voltage, $\zeta(x)$ is the hysteresis transit variable, V_{gap} is the hysteresis half-gap,²⁴ and R_1, R_2, \dots are the Taylor coefficients. We are assuming that temperature is held constant, and that OCV does not change with age.

Ideally, we would directly measure OCV and V_{gap} for the cell under study using a C/100 cycle, but lacking that, we must estimate it from the data on hand. First, we assume that $V_{gap} \equiv 0$, which is reasonably accurate since most NMC formulations have a hysteresis half-gap of approximately 5 mV over the range of 10% to 100% SOC, with some increase below 10%SOC. Second, we assume that the higher-order terms in current are negligible, so that Eq. 1 simplifies to Eq. 2:

$$V(x) \approx OCV(x) + R(x, Q_{tot})\hat{I}, \quad [2]$$

where we will refer to $R(x, Q_{tot})$ as the normalized resistance, having units of Vh. By definition, during discharge, the state of charge coordinate is described in Eq. 3:

$$x_i^D(t) = 1 + \frac{q_i^D(t)}{Q_{tot_i}}. \quad [3]$$

During the subsequent charge, we compensate for Coulombic inefficiency by using Eq. 4:

$$x_i^C(t) = 1 + \frac{q_i^C(t)}{Q_{tot_i} + (Q_{CCi}^C - Q_{CCi}^D)}. \quad [4]$$

Since by definition $Q_{tot_{i0}} = Q_{CC10}^D$, one may confirm that both x_{i0}^D and x_{i0}^C range from 0 to 1, hitting those limits precisely. In both cases, $q(t)$ and hence $x(t)$ are monotonic with respect to t , so once Q_{tot_i} is determined, the measured voltage response $[V(t), x(t)]$ can be interpolated to provide $V(x)$.

Assuming that Eq. 2 applies to both charge and discharge,

$$V^D(x) = OCV(x) + R(x, Q_{tot})\hat{I}^D, \quad V^C(x) = OCV(x) + R(x, Q_{tot})\hat{I}^C, \quad [5]$$

we can estimate the OCV function using the initial cycle in Eq. 6:

$$OCV(x) = \frac{\hat{I}^C(x)V^D(x) - \hat{I}^D(x)V^C(x)}{\hat{I}^C - \hat{I}^D} \quad [6]$$

To compute this from the time-sampled data, one must interpolate the time-sampled discharge data $V^D(t)$, $q^D(t)$ and time-sampled charge data $V^C(t)$, $q^C(t)$ to common SOC points, x , using Eqs. 3,4. This can only be done at the initial cycle #10, where we know $Q_{tot_{i0}}$. In our experiments, we used C-rates of $\hat{I}^C = 0.1/h$ and $\hat{I}^D = -0.5/h$. Hence, the OCV curve closely follows $V^C(x)$.

Total capacity and normalized resistance.—With $OCV(x)$ estimated from the initial cycle, the normalized resistance for the i th discharge cycle is described in Eq. 7:

$$R(x, Q_{tot_i}) = \frac{V_i^D(x) - OCV(x)}{\hat{I}_i^D}, \quad x = x_i^D = 1 + \frac{q_i^D(t)}{Q_{tot_i}}, \quad \hat{I}_i^D = \frac{I^D}{Q_{tot_i}}. \quad [7]$$

To evaluate $R(x, Q_{tot_i})$, we need to know Q_{tot_i} . At the start, we only know $Q_{tot_{i0}}$ for our initial cycle. For subsequent cycles, we need to jointly estimate Q_{tot_i} and $R(x, Q_{tot_i})$, where the resistance function is unknown. To proceed, we consider cycles close to each other, that is we consider cycles i and $j > i$ where $j - i$ is small. For such cycles, we assume that the resistance grows by the same proportion across the SOC range, which we write as Eq. 8:

$$R(x, Q_{tot_j}) \approx \rho_{ij}R(x, Q_{tot_i}). \quad [8]$$

where ρ_{ij} is the proportionality factor. With this assumption, the voltage model for the j th discharge becomes Eq. 9:

$$V_j^D(x_j^D, Q_{tot_j}) = OCV(x_j^D) + \rho_{ij}R(x_j^D, Q_{tot_i})\hat{I}_j^D, \quad x_j^D = 1 + \frac{q_j^D(t)}{Q_{tot_j}}, \quad \hat{I}_j^D = \frac{I_j^D}{Q_{tot_j}} \quad [9]$$

If $R(x, Q_{tot_i})$ is known, then we can estimate Q_{tot_j} and ρ_{ij} to match this model to the measured voltage for the j th discharge in Eq. 10:

$$\min_{Q_{tot_j}, \rho_{ij}} \sum_k e_{ij,k}^2, \quad e_{ij,k} = OCV(x_{jk}^D) + \rho_{ij}R(x_{jk}^D, Q_{tot_i})\hat{I}_j^D - V_{jk}^D \quad [10]$$

where subscript k means the k th sample in the measured discharge curve. With an initial estimation of $Q_{tot_j} = Q_{tot_i}$ and $\rho_{ij} = 1$, a gradient descent method converges quickly to a minimum. After estimating Q_{tot_j} by this procedure, we use Eq. 7 to compute $R(x, Q_{tot_j})$, which prepares us to iterate the procedure for the next value of j , as illustrated in Fig. S2.

We do not expect Eq. 8 to be a good approximation for widely separated cycles, $j \gg i$. Instead, we proceed in small steps of 10 cycles, $(i, j) = (10, 20), (20, 30), \dots$, until near the point where rapid capacity loss begins, at which point we iterate in steps of 1. For Cell #1, rapid loss starts earlier, around cycle 308 (Fig. 3, so the end of the sequence is $(i, j) = \dots, (290, 300), (300, 303), (303, 304), \dots, (309, 310)$. For Cell #2, whose rapid capacity loss starts around cycle 390 (Fig. 3), the iterations switch from steps of 10 to steps of 1 at cycle 385, i.e., $(i, j) = \dots, (370, 380), (380, 385), (385, 386), \dots, (391, 392)$. In either case, there is no motivation to continue more than 2 cycles beyond the onset of failure.

For illustration, consider the first step from cycle 10 to cycle 20 for Cell #2. We start with $Q_{tot_{i0}} = 4.420Ah$, and the fitting process returns $Q_{tot_{20}} = 4.409Ah$, $\rho_{10,20} = 1.03$. This indicates that the 15mAh drop in the CC capacity from $Q_{CC10}^D = 4420mAh$ to $Q_{CC20}^D = 4405mAh$, is a combination of an 11mAh drop in the total capacity and an average increase in resistance of 3%. The error in this fit is shown in Fig. S2, plotted as $e_{ij,k}$ vs $x_{20,k}^D$. The RMS error of the fit is 4.6 mV, with most of the error occurring near the ends of the SOC range, where the slope of the curve accentuates errors. The low, flat error in the middle SOC range indicates that the capacity has been matched well, while the error near the ends of SOC tell us

that the resistance function $R(x, Q_{tot})$ is evolving in a way that is not perfectly matched by a simple proportional growth. This is expected, and in fact, this is why we update $R(x, Q_{tot})$ using Eq. 7 each time before extending the fit to the next Q_{totj} using Eq. 8.

After the sequence of fits provides an estimate of Q_{toti} for every cycle i , we can compare voltages between cycles on a plot vs SOC. Figures 5 and S3 show the voltage curves for both cells. For most cycles, the fitted curves (dotted) are indistinguishable from the measured ones (solid).

The fitting process is stopped two cycles beyond the onset of rapid capacity loss. This is because the assumptions inherent in Eqs. 8, 9 can no longer be justified. Specifically, Eq. 8 assumes that resistance grows by a constant factor, ρ_{ij} , across all SOC from one cycle to the next, while Eq. 9 assumes that the same capacity Q_{toti} is valid for the entire discharge cycle. Once the sudden capacity loss began, the characteristics of the cell changed significantly within a single cycle.

After the fitting process, we can also evaluate $R(x, Q_{toti})$ for each cycle via (7). These curves are plotted vs SOC in Figs. S4 and S5. For head-to-head comparison, Fig. 6 shows the resistance at 50% SOC, *i.e.*, $R(0.5, Q_{toti})$, which we label $R_{50\%}$, along with capacities, both plotted against cycle number. The arrows indicate the last cycle before the onset of rapid capacity loss. Acceleration in the rate of resistance growth suggests that the electrolyte was either degrading or being consumed, while the sudden downturn in capacity suggests that some of the cathode material is rapidly falling out of use, likely because some particles are no longer wetted by electrolyte. Cell #1, which started with the least electrolyte, enters the acceleration phase earlier. All three cells began failing at similar values of normalized resistance. While the capacities for the two cells follow a similar trend line, the resistance of Cell #1 (red triangles) grows more quickly than that for Cells #2 and #3, which are depicted as blue and yellow triangles, respectively. For all the cells, growth in the resistance accelerates as the capacity began to fail. Annotations indicate the value of $R_{50\%}$ at the onset of failure. The results for Cells

#2 and #3 are nearly identical, which indicates that there is no effect in adding electrolyte beyond 2.2 g Ah^{-1} . Evidently when any cell of this type is placed under pressure and sealed, its porous structure can hold a maximum of about 2.2 g Ah^{-1} ; the rest is ejected during the sealing process. In sum, by modelling the voltage curves and capacity, we can conclude that the onset sudden loss of capacity is in concurrence with the emergence of resistance acceleration. Although the pouch cell (Cell #2 and Cell #3) with higher amount of electrolyte displayed longer cycle life, this correlation between sudden loss of capacity and cell resistance acceleration is independent of the electrolyte amount used in the pouch cells.

Post-mortem scanning electron microscope (SEM) analysis.— After 395 cycles, the aged anode, cathode, and electrolyte of Cell #2 were harvested and studied to understand the build-up of resistance during cycling and the mechanism behind the sudden capacity loss. The scanning electron microscope (SEM) images in Fig. 7 depict the cross-section of the anode harvested from the pouch cell after 400 cycles (Fig. 7a) and the pristine anode (Fig. 7b). Compared to the pristine $20 \mu\text{m}$ Li metal electrode, the thickness of aged anode increased dramatically. This result is consistent with previous publications stating that after cycling, Li anodes become porous, sometimes referred to as “mossy lithium.”^{35–37} The formation of mossy lithium results in several effects. First, the increase in porosity compared to pristine lithium anode means it can capture more electrolyte, which may pull electrolyte out of the cathode and separator. Second, it may promote the consumption of electrolyte in forming new SEI originated by the greater contact area between Li and the electrolyte. Third, the continuous cycles of plating and stripping as the cell charges and discharges disrupts the formation of a stable SEI layer to protect the anode, thus allowing further consumption of electrolyte even after the transformation to the mossy condition is complete.

The harvested cathodes were also studied by SEM, and representative images shown in Fig. 8. The cross-sections in Figs. 8a and 8c show a thickness of $80 \mu\text{m}$ for both samples: no dramatic

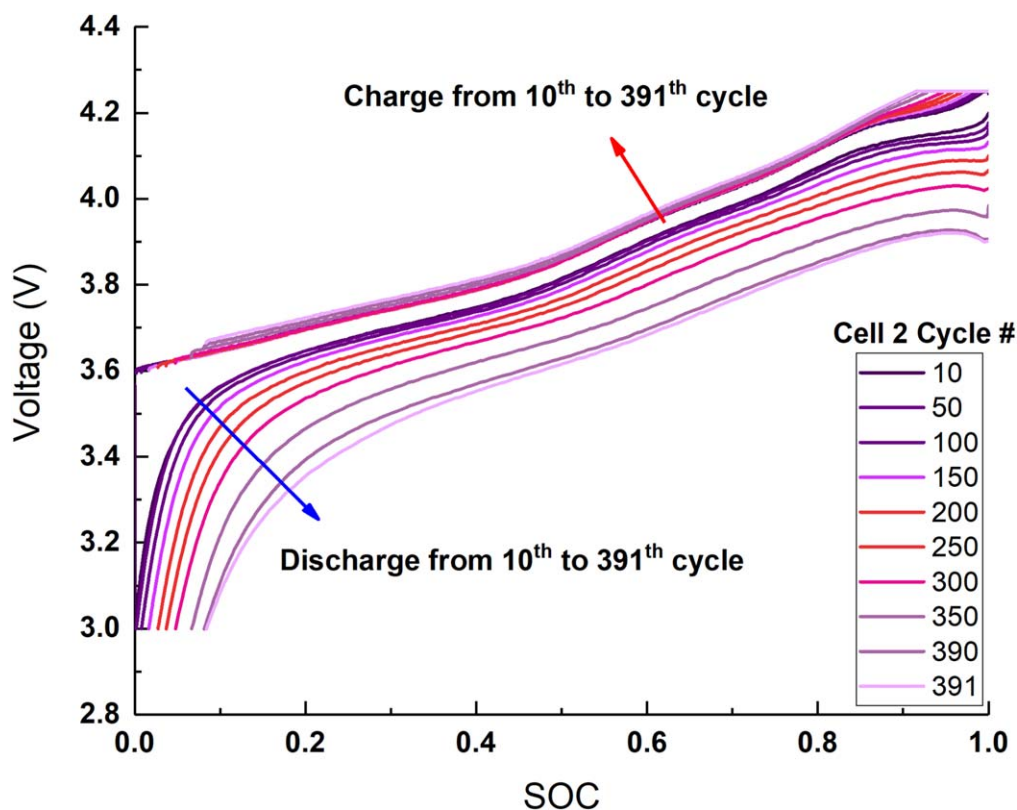


Figure 5. Cell #2: Voltage vs SOC for selected cycles. Solid lines are measured voltage; dotted lines are the corresponding fits.

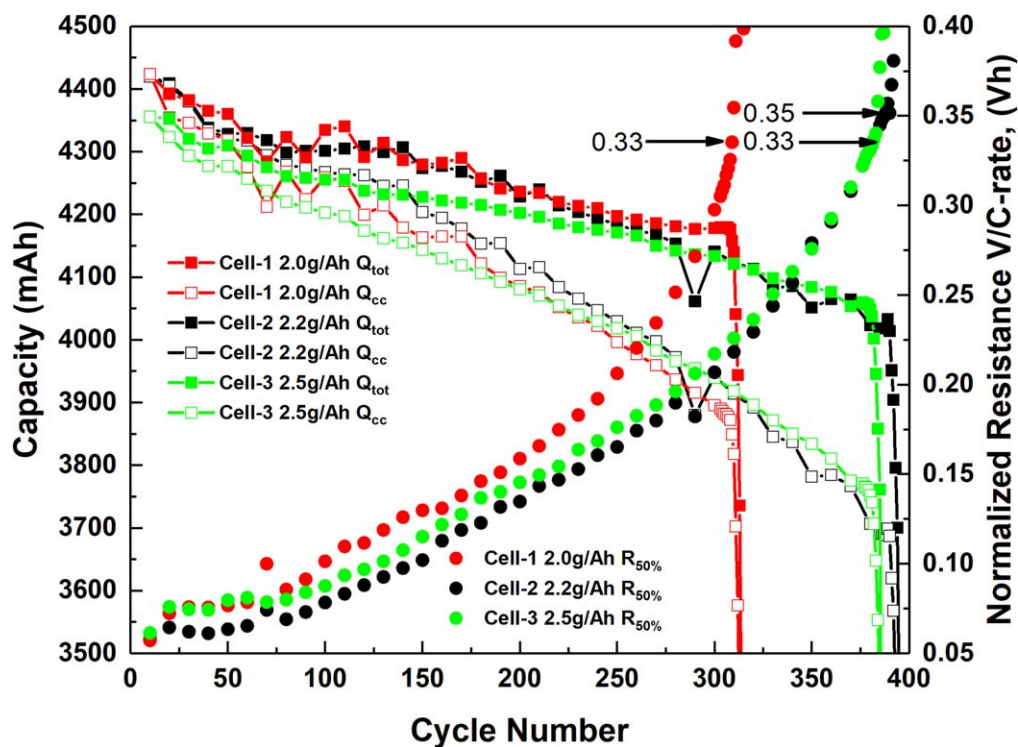


Figure 6. Total and constant-current capacities and $R_{50\%}$ vs cycle number.

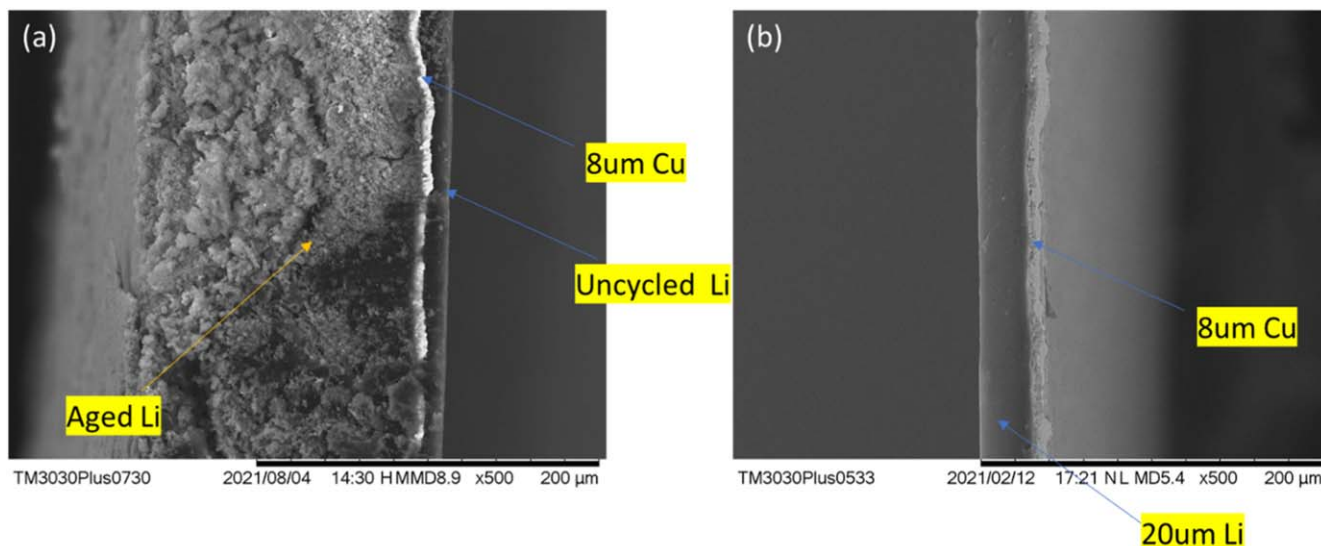


Figure 7. SEM images of Li anode before and after 400 cycles (Cell #2): (a). aged Li metal anode and (b) pristine Li metal anode.

difference in thickness is seen. The top views of Figs. 8b and 8d show some micro-cracks, which denoted by arrows, on the aged sample, not present on the pristine one. Those cracks are not expected to affect the performance of cathode dramatically.

X-ray diffraction (XRD) analysis.—X-ray diffraction (XRD) was further employed to quantify the structural changes of the cathode lattice during cycling. Figure 9a compares the XRD pattern of pristine and aged cathode after 400 cycles. All aged samples were discharged to 2.5 V and held for 2 h before the XRD scanning. The XRD diffraction peaks of both pristine and aged NMC samples exhibit sharp, well-defined Bragg lines corresponding to a rhombohedral structure, consistent with α - NaFeO_2 (space group: $R\bar{3}m$). Under the resolution utilized by the diffractometer, there is no

evidence for the existence of a secondary phase in any of the samples. The small shift of (003) and (101) peaks indicated in Figs. 9b and 9c can be attributed to the loss of active Li in the NMC811 lattice structure. Also, the splitting of peaks (108) and (110) originates from the increasing Li-Ni cation mix percentage upon cycling. Those tiny changes on the XRD pattern imply that the cathodes have only limited structural changes upon cycling, so cathode degradation should not be the cause of the sudden capacity loss of the LMBs.

Post-test capacity analysis.—To investigate the condition of the cathode aged to end-of-life (EOL) at 400 cycles, we cut a disk from the harvested cathode and built a coin cell using a fresh lithium anode, electrolyte, and separator. Figure 10 compares a coin cell

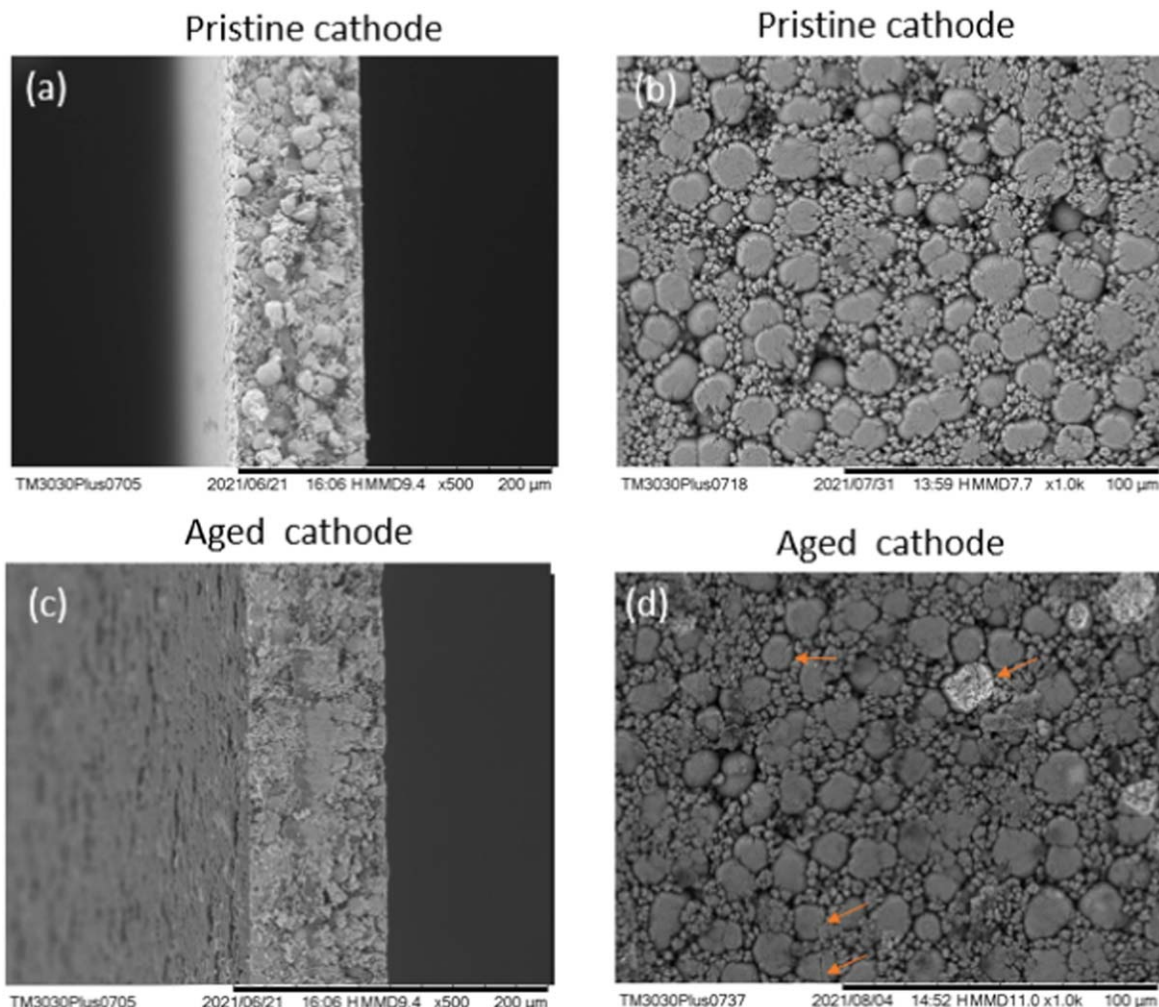


Figure 8. SEM images of the cathode before (a), (b) and after (c), (d) 400 cycles: (a), (c). Cross sections and (b), (d) top views.

built with fresh anode and cathode to that with an aged cathode. In Fig. 10a, for a 0.1 C charge and discharge rate between the 3.0–4.25 V operation window, the fresh coin cell delivered 235 mAh/g specific capacity, while the coin cell with an aged cathode at the EOL delivered only 195 mAh g⁻¹ discharge capacity as shown in Fig. 10b. However, when the current rate was reduced to C/50, 220 mAh g⁻¹ capacity was obtained, which was close to the capacity delivered by a fresh cathode. The ratio between the C/10 discharge capacities for the fresh and aged cathodes in these coin cells is 195/235 ≈ 85%. The ratio between the C/2 discharge capacities of pouch Cell #2 at cycle 390 (just before the onset of capacity collapse) was comparable at 3687/4425 ≈ 83% while the ratio for the final cycle 395 was a much smaller 3000/4425 ≈ 68%. That is, when placed opposite fresh anode and provided with fresh electrolyte, the aged cathode recovered to a capacity comparable to its value just before the onset of capacity collapse. This indicates that the cycled cathode has limited lattice damage, in concordance with the XRD results above. Clearly, most of the capacity loss from the cathode side is because of the impedance build-up.

A similar study was also carried out for the cycled anode to investigate the source of capacity collapse. The Li anode aged to EOL at 400 cycles was harvested from pouch Cell #2 and reassembled with fresh cathode, electrolyte, and separator. The voltage plot in Fig. 11 shows that the as-assembled coin cell still delivered 240 mAh g⁻¹ discharge capacity under the current rate of C/50 between 3.0–4.25 V operation window. This exceeds the C/10 discharge capacity of 235 mAh/g for a fresh coin cell, thereby indicating that the lithium remaining in the cycled anode was still

sufficient to exercise the entire capacity of the cathode. We also carried out additional study to verify our hypothesis that electrolyte dry-out is the main reason of the sudden capacity drop by replenishing 30 μl fresh electrolyte into a disassembled Li/NMC cell cycled to EOL at 300 cycles and reassembling the cell with fresh electrolyte but aged lithium anode, cathode and separator. The voltage profile in Fig. 11 shows that the reassembled coin cell still delivered 210 mAh g⁻¹ discharge capacity under the current rate of C/10 between 3.0–4.25 V operation window. This result again supports the electrolyte dry-out hypothesis. Taken together, these coin cell results show that the sudden capacity loss at EOL arose from neither the loss of active material in the cathode, nor the loss of lithium in the anode. While the coin cell with aged cathode displayed increased impedance, its effect on constant-current capacity appeared to be comparable to the capacity lost by the pouch cell up to the onset of capacity collapse. This conclusion is supported by the results of the capacity tests for the coin cell and the cycling performance of the pouch cell at different C-rates. The increased impedance is probably caused by the presence of products deposited during electrolyte decomposition. However, this impedance growth did not cause the final precipitous decline of capacity. Therefore, electrolyte failure arising from electrolyte decomposition and its eventual dry-out is the remaining suspect.

Quantitative analysis of electrolyte after cycling.—To further understand the change of electrolyte upon cycling, nuclear magnetic resonance (NMR) was applied to quantitatively analyze the harvested electrolyte samples. Figures S6 and S7 show the ¹H and ¹⁹F

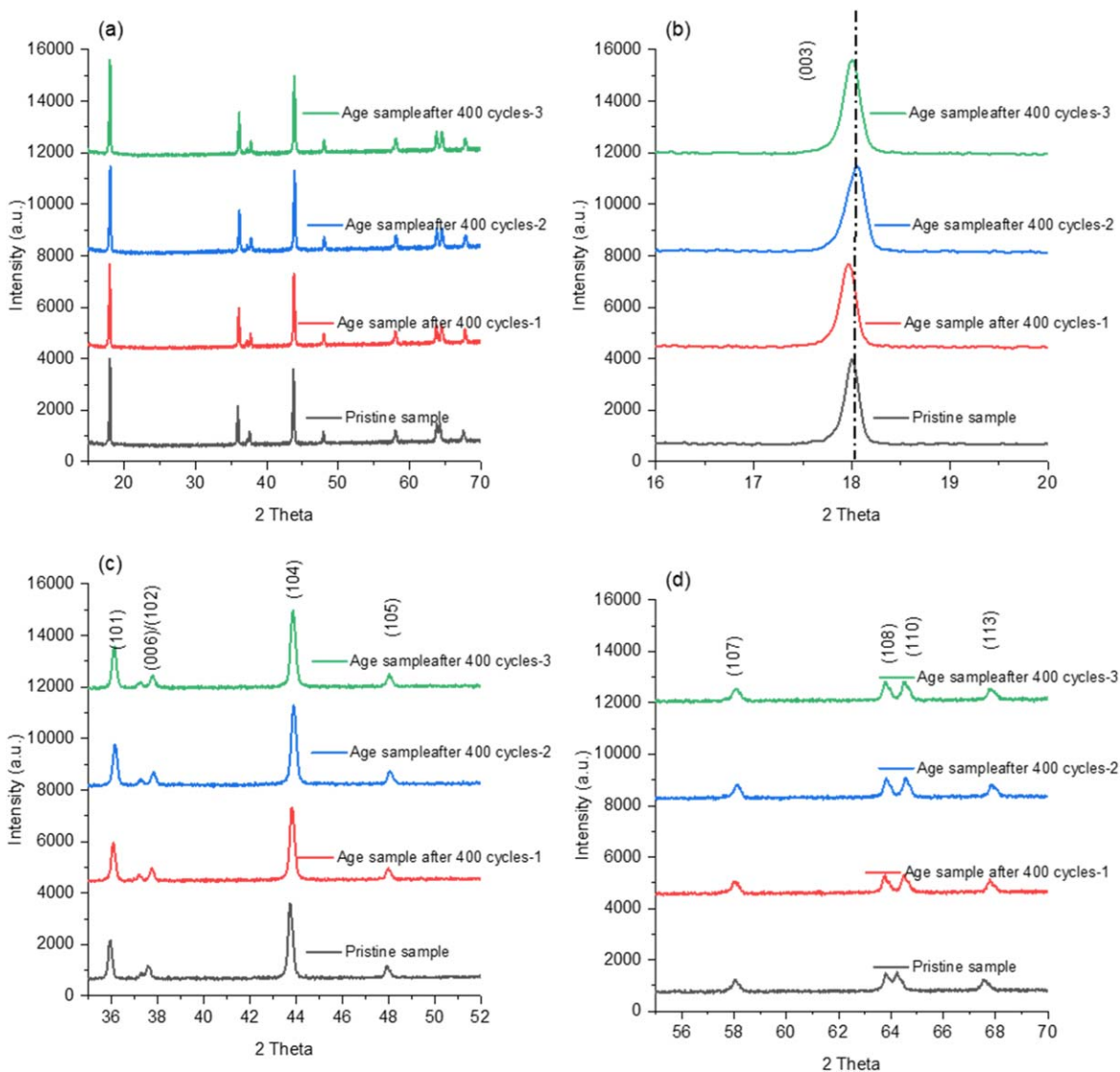


Figure 9. XRD patterns of pristine and aged cathode sample: (a) the whole scanning range, (b) (003) peak position, (c) (101) peak position and (d) (108) and (110) peak position.

NMR spectra of the electrolyte harvested from the 5Ah Cell #2 after 400 cycles. No FEC was detected and the amount of DMC was nearly negligible, corroborating our speculation that the electrolyte had dried out at the end of cycle life. The ^{19}F spectrum also shows that the amount of LiPF_6 extracted was very low, further confirming our hypothesis. Coin cells with $30\ \mu\text{l}$ electrolyte amount were prepared and subjected to the cycling test. Figure S8 shows that the capacity retention of the coin cell follows the same trend as the pouch cells up to 300 cycles, at which the coin cell was disassembled to quantify the amount of remaining electrolyte. To establish a baseline for the fresh condition, $30\ \mu\text{l}$ of fresh electrolyte was dissolved in 3 mL acetonitrile- d_3 and tested by NMR, and subsequently, the electrolyte remaining in the aged coin cell was harvested using the same solvent and quantity, *i.e.* 3 mL acetonitrile- d_3 , thus making the NMR results comparable. ^1H and ^{19}F NMR spectra for the fresh electrolyte are shown in Figs. 12 and S9, respectively, and the corresponding results for the aged electrolyte are shown in Figs. 13 and S10, with the details summarized in Table I. The molar ratio of FEC to DMC changed from 1:3 to 1:2, showing that DMC decomposed faster than FEC. Since all CD_2HCN comes from the same 3 mL of solvent, its total mass is the same in both samples; hence, the change in the molar ratio of DMC to CD_2HCN from 1:6 to 1:22 reveals that about 72% of the DMC has decomposed during

the cycling. The molar ratio of LiPF_6 to FEC changed from 1:1.4 to 1:0.54, indicating that FEC decomposed at a faster rate than the consumption of LiPF_6 salt. Finally, the semi-quantified volume of electrolyte reduced from $30\ \mu\text{l}$ to just $12\ \mu\text{l}$ during the cycling. These results tell us the rate of decomposition of the electrolyte and its individual components up to the 300th cycle, *i.e.*, before the onset of sudden capacity failure. Apparently, the fast electrolyte consumption was the major cause for the cell failure, initiated by electrolyte decomposition and dry-out. For example, if we assume DMC was consumed at a constant rate every cycle, and we knew that 28% of DMC remained at 300 cycles, then we are able to estimate that DMC will be totally consumed by cycle 420. Although, the electrolyte consumption rate may vary as the balance of the species present in the electrolyte changes, the results were still highly consistent with the hypothesis that the sudden failure of the cell was caused by electrolyte dry-out.

Conclusions

All in all, three 5Ah pouch-cell Lithium Metal Batteries (LMBs) were built using different electrolyte injection amounts, 2.5, 2.2, and $2.0\ \text{g Ah}^{-1}$, respectively, and then cycled to the end of life (EOL). An analysis of the voltage curves collected during cycling indicated

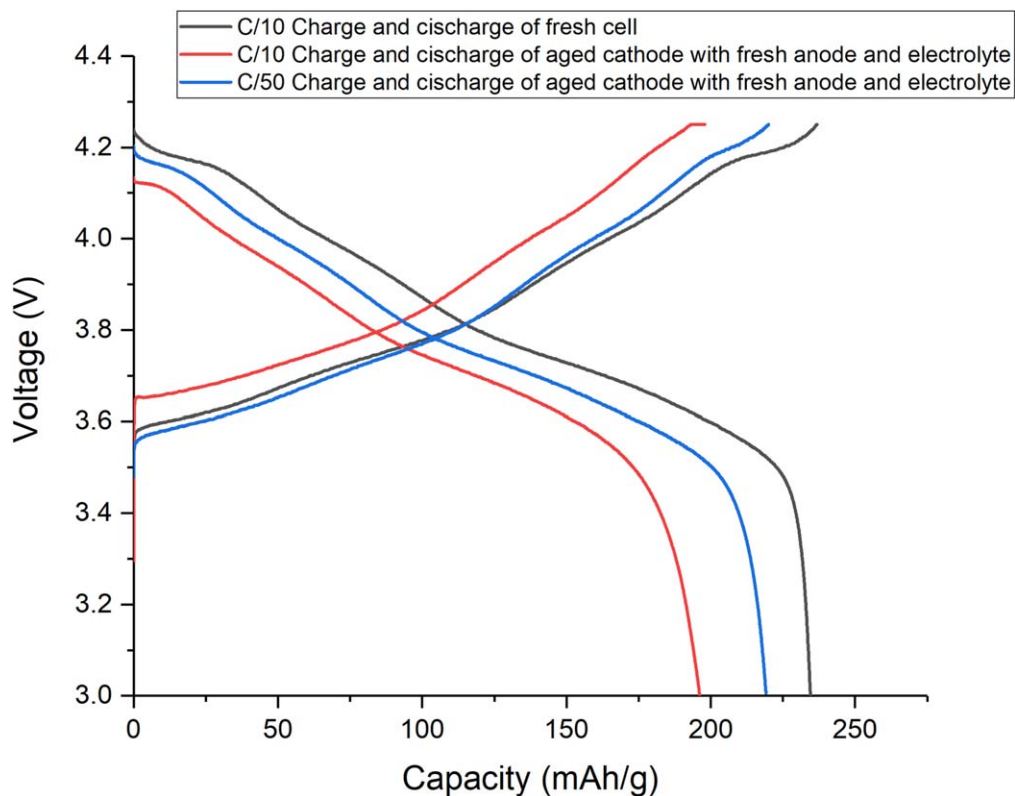


Figure 10. The voltage profile comparison of fresh assembled coin cell and the reassembled aged cathode/anode with fresh electrolyte coin cell.

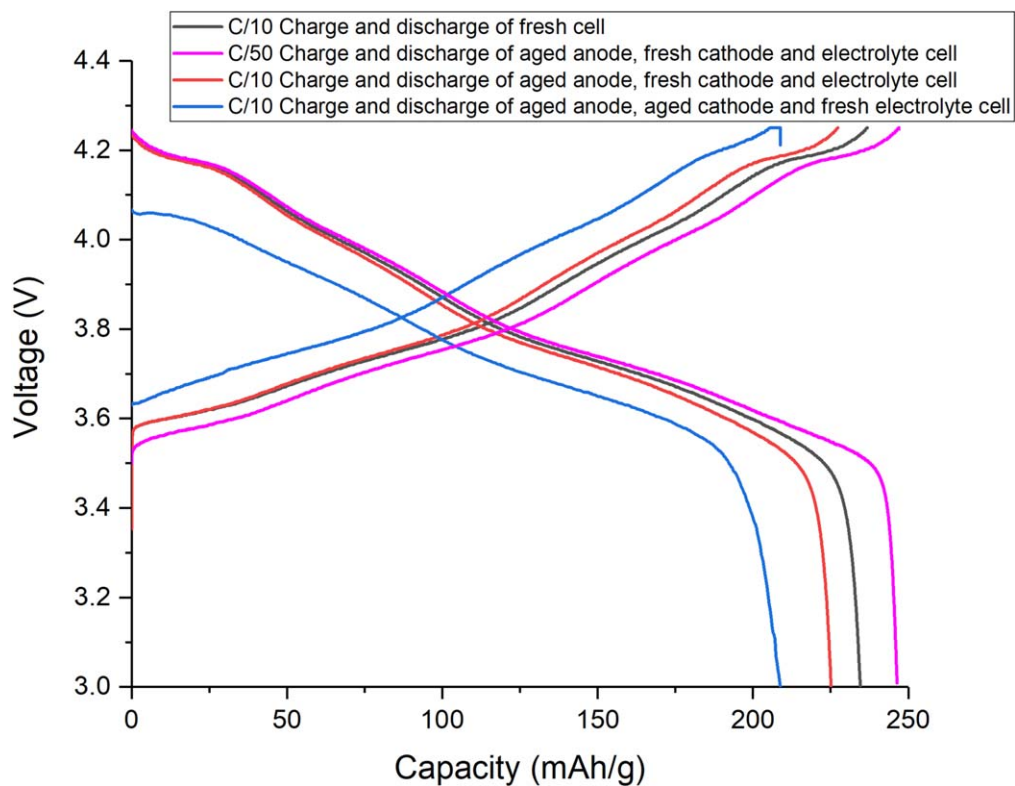
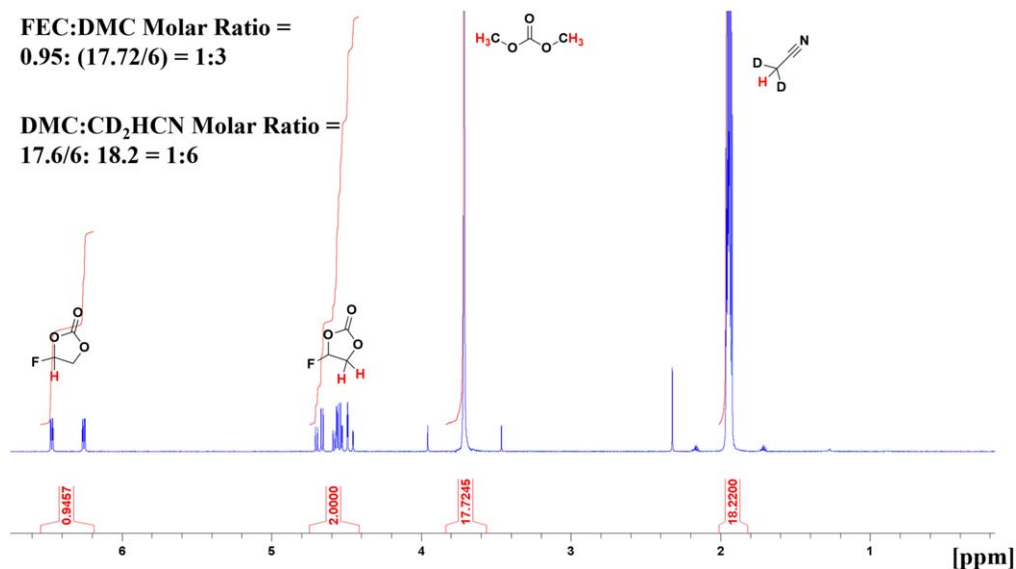
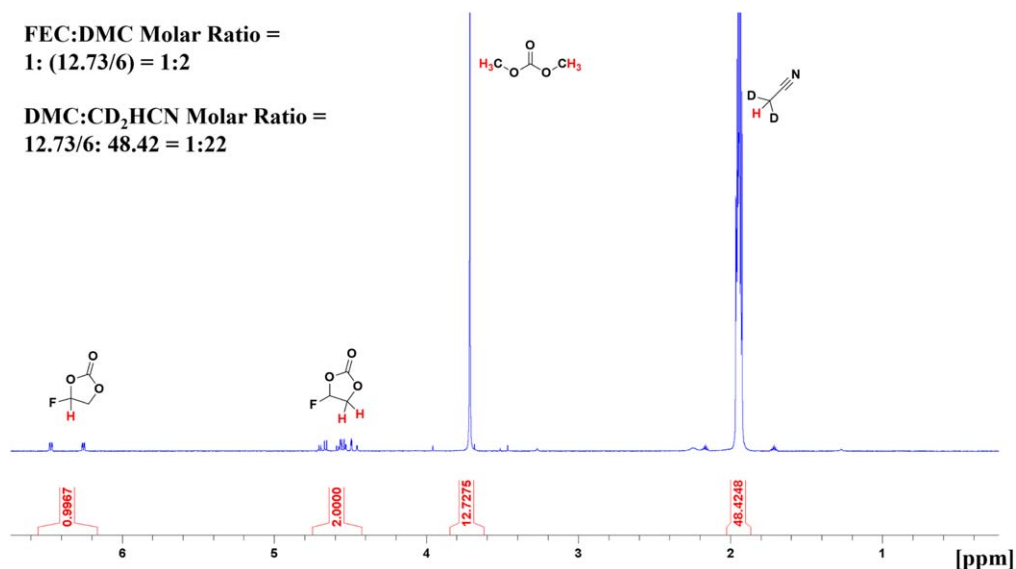


Figure 11. The voltage profile comparison of fresh as-assembled coin cell and as-reassembled aged cathode/anode with fresh electrolyte coin cell.

that the cathode capacity declined in a linear fashion while the resistance grew at an accelerating rate. The capacity degradation for a pouch cell assembled with 2.0 g Ah^{-1} of electrolyte followed the

same trend as for ones with more electrolyte, 2.2 g Ah^{-1} and 2.5 g Ah^{-1} , but the resistance acceleration of the one with less electrolyte happened at a lower cycle number, leading to earlier cell

Figure 12. ¹H-NMR spectrum of fresh electrolyte.Figure 13. ¹H-NMR spectrum of harvested electrolyte after 300 cycles.**Table I.** NMR molar ratios and semi-quantified volume of electrolyte for a fresh coin cell and as harvested from a coin cell aged 300 cycles.

| | Fresh electrolyte | Aged electrolyte |
|-------------------------------------|-------------------|------------------|
| Molar ratio FEC:DMC | 1:3 | 1:2 |
| Molar ratio DMC:CD ₂ HCN | 1:6 | 1:22 |
| Molar ratio LiPF ₆ :FEC | 1:1.4 | 1:0.54 |
| Electrolyte volume | 30 μl | 12 μl |

failure. All three pouch cells showed a dramatic increase in resistance leading up to capacity failure and each subsequently failed at nearly the same normalized resistance. These results are consistent with the hypothesis that the culprit of cell failure is the depletion of electrolyte since resistance is expected to grow as electrolyte dries out. Our hypothesis was further confirmed by a variety of post-mortem analyses. It was discovered that the anode still contains active lithium approaching the EOL, evidenced by the

normal capacity delivered by the cell using fresh NMC cathode and aged lithium anode. Also, when assembled with fresh anode and electrolyte, an aged cathode delivered reasonable capacity but showed increased resistance compared to a pristine one. Although there was a decrease in the specific capacity of the aged cathode, our XRD results showed that there was no dramatic lattice damage. NMR analysis of the electrolyte showed significant decomposition at 300 cycles of a coin cell and near total consumption at the EOL of a pouch cell. These results indicate that decomposition and consumption of the electrolyte is the main cause of this sudden capacity failure.

Acknowledgments

The authors gratefully acknowledge support from the General Motors Inc. Argonne National Laboratory is operated by DOE Office of Science by UChicago Argonne, LLC, under contract number DE-AC02-06CH11357. Conflicts of interest. There are no conflicts of interest to declare.

ORCID

Chi-Cheung Su  <https://orcid.org/0000-0001-5675-3173>

References

- B. Liu, J.-G. Zhang, and W. Xu, "Advancing lithium metal batteries." *Joule*, **2**, 833 (2018).
- J. Liu et al., "Pathways for practical high-energy long-cycling lithium metal batteries." *Nat. Energy*, **4**, 180 (2019).
- X. Shen, H. Liu, X.-B. Cheng, C. Yan, and J.-Q. Huang, "Beyond lithium ion batteries: Higher energy density battery systems based on lithium metal anodes." *Energy Storage Mater.*, **12**, 161 (2018).
- Y. Qiao, H. Deng, P. He, and H. Zhou, "A 500 Wh/kg lithium-metal cell based on anionic redox." *Joule*, **4**, 1445 (2020).
- B. Han et al., "500 Wh kg⁻¹ class Li metal battery enabled by a self-organized core-shell composite anode." *Adv. Mater.*, **32**, 2004793 e2004793 (2020).
- M. S. Park, S. B. Ma, D. J. Lee, D. Im, S. G. Doo, and O. Yamamoto, "A highly reversible lithium metal anode." *Sci. Rep.*, **4**, 3815 (2014).
- Q. Zhao, X. Chen, W. Hou, B. Ye, Y. Zhang, X. Xia, and J. Wang, "A facile, scalable, high stability Lithium metal anode." *SusMat*, **2**, 104 (2022).
- S. Park, H. J. Jin, and Y. S. Yun, "Advances in the design of 3D-Structured electrode materials for lithium-metal anodes." *Adv. Mater.*, **32**, 2002193 e2002193 (2020).
- X. Zhang, A. Wang, X. Liu, and J. Luo, "Dendrites in lithium metal anodes: suppression, regulation, and elimination." *Acc. Chem. Res.*, **52**, 3223 (2019).
- F. Wu, Y.-X. Yuan, X.-B. Cheng, Y. Bai, Y. Li, C. Wu, and Q. Zhang, "Perspectives for restraining harsh lithium dendrite growth: towards robust lithium metal anodes." *Energy Storage Mater.*, **15**, 148 (2018).
- L. Frenck, G. K. Sethi, J. A. Maslyn, and N. P. Balsara, "Factors that control the formation of dendrites and other morphologies on lithium metal anodes." *Frontiers in Energy Research*, **7**, 1–11 (2019).
- X. Shen, R. Zhang, X. Chen, X. B. Cheng, X. Li, and Q. Zhang, "The failure of solid electrolyte interphase on Li metal anode: structural uniformity or mechanical strength?" *Adv. Energy Mater.*, **10**, 1903645 (2020).
- K. Liu, M. Wu, H. Jiang, Y. Lin, and T. Zhao, "An ultrathin, strong, flexible composite solid electrolyte for high-voltage lithium metal batteries." *J. Mater. Chem. A*, **8**, 18802 (2020).
- Z. Yu et al., "A solution-processable high-modulus crystalline artificial solid electrolyte interphase for practical lithium metal batteries." *Adv. Energy Mater.*, **12**, 2201025 (2022).
- Q. Li, S. Zhu, and Y. Lu, "3D porous Cu current collector/Li-Metal composite anode for stable lithium-metal batteries." *Adv. Funct. Mater.*, **27**, 1606422 (2017).
- D. Zhang, A. Dai, M. Wu, K. Shen, T. Xiao, G. Hou, J. Lu, and Y. Tang, "Lithiophilic 3D porous CuZn current collector for stable lithium metal batteries." *ACS Energy Lett.*, **5**, 180 (2019).
- C. Chen, S. Li, P. H. L. Notten, Y. Zhang, Q. Hao, X. Zhang, and W. Lei, "3D Printed Lithium-metal full batteries based on a high-performance three-dimensional anode current collector." *ACS Appl. Mater. Interfaces*, **13**, 24785 (2021).
- Z. Hao, Q. Zhao, J. Tang, Q. Zhang, J. Liu, Y. Jin, and H. Wang, "Functional separators towards the suppression of lithium dendrites for rechargeable high-energy batteries." *Mater Horiz.*, **8**, 12 (2021).
- X. Q. Zhang, X. Chen, X. B. Cheng, B. Q. Li, X. Shen, C. Yan, J. Q. Huang, and Q. Zhang, "Highly stable lithium metal batteries enabled by regulating the solvation of lithium ions in nonaqueous electrolytes." *Angew. Chem. Int. Ed. Engl.*, **57**, 5301 (2018).
- F.-N. Jiang, S.-J. Yang, X.-B. Cheng, P. Shi, J.-F. Ding, X. Chen, H. Yuan, L. Liu, J.-Q. Huang, and Q. Zhang, "Thermal safety of dendritic lithium against nonaqueous electrolyte in pouch-type lithium metal batteries." *Journal of Energy Chemistry*, **72**, 158 (2022).
- J. G. Zhang, W. Xu, J. Xiao, X. Cao, and J. Liu, "Lithium metal anodes with nonaqueous electrolytes." *Chem. Rev.*, **120**, 13312 (2020).
- A. Nakanishi, K. Ueno, D. Watanabe, Y. Ugata, Y. Matsumae, J. Liu, M. L. Thomas, K. Dokko, and M. Watanabe, "Sulfolane-based highly concentrated electrolytes of lithium Bis(trifluoromethanesulfonyl)amide: ionic transport, Li-Ion coordination, and Li-S battery performance." *The Journal of Physical Chemistry C*, **123**, 14229 (2019).
- L. Dong et al., "Stabilization of high-voltage lithium metal batteries using a sulfone-based electrolyte with bi-electrode affinity and LiSO₂F-rich interphases." *Energy Storage Mater.*, **44**, 527 (2022).
- R. Marrache, T. Mukra, and E. Peled, "Elucidation of losses in cycling lithium-metal anodes in ether-based electrolytes." *J. Electrochem. Soc.*, **170**, 040512 (2023).
- S. Atalay, M. Sheikh, A. Mariani, Y. Merla, E. Bower, and W. D. Widanage, "Theory of battery ageing in a lithium-ion battery: capacity fade, nonlinear ageing and lifetime prediction." *J. Power Sources*, **478**, 229026 (2020).
- L. Su, H. Charalambous, Z. Cui, and A. Manthiram, "High-efficiency, anode-free lithium-metal batteries with a close-packed homogeneous lithium morphology." *Energy Environ. Sci.*, **15**, 843 (2022).
- H. Li, D. Chao, B. Chen, X. Chen, C. Chuah, Y. Tang, Y. Jiao, M. Jaroniec, and S. Z. Qiao, "Revealing principles for design of lean-electrolyte lithium metal anode via *In Situ* spectroscopy." *J. Am. Chem. Soc.*, **142**, 2012 (2020).
- W. Deng, X. Yin, W. Bao, X. Zhou, Z. Hu, B. He, B. Qiu, Y. S. Meng, and Z. Liu, "Quantification of reversible and irreversible lithium in practical lithium-metal batteries." *Nat. Energy*, **7**, 1031 (2022).
- S. C. Nagpure, T. R. Tanim, E. J. Dufek, V. V. Viswanathan, A. J. Crawford, S. M. Wood, J. Xiao, C. C. Dickerson, and B. Liaw, "Impacts of lean electrolyte on cycle life for rechargeable Li metal batteries." *J. Power Sources*, **407**, 53 (2018).
- P. Daubinger, M. Göttlinger, S. Hartmann, and G. A. Giffin, "Consequences of different pressures and electrolytes on the irreversible expansion of lithium metal half cells." *Batteries & Supercaps*, **6**, e20220045 (2022).
- D. Lu et al., "Failure mechanism for fast-charged lithium metal batteries with liquid electrolytes." *Adv. Energy Mater.*, **5**, 1400993 (2015).
- F. Ahmad, A. Iqbal, I. Ashraf, M. Marzband, and I. Khan, "Optimal location of electric vehicle charging station and its impact on distribution network: a review." *Energy Reports*, **8**, 2314 (2022).
- R. German, S. Shili, A. Desrevaux, A. Sari, P. Venet, and A. Bouscayrol, "Dynamical coupling of a battery electro-thermal model and the traction model of an EV for driving range simulation." *IEEE Trans. Veh. Technol.*, **69**, 328 (2020).
- W. Kempton, "Electric vehicles: driving range." *Nat. Energy*, **1**, 16131 (2016).
- C.-J. Ko, C.-H. Chen, and K.-C. Chen, "Influence of inhomogeneity of lithium-ion transport within the anode/electrolyte interface on mossy lithium formation." *J. Power Sources*, **563**, 232779 (2023).
- Y. Shi, Z. Wang, H. Gao, J. Niu, W. Ma, J. Qin, Z. Peng, and Z. Zhang, "A self-supported, three-dimensional porous copper film as a current collector for advanced lithium metal batteries." *J. Mater. Chem. A*, **7**, 1092 (2019).
- X.-R. Chen, C. Yan, J.-F. Ding, H.-J. Peng, and Q. Zhang, "New insights into 'dead lithium' during stripping in lithium metal batteries." *Journal of Energy Chemistry*, **62**, 289 (2021).